

Structure and function of human XPR1 in phosphate export

Received: 19 August 2024

Accepted: 13 March 2025

Published online: 26 March 2025

 Check for updatesLong Chen^{1,2}, Jin He^{1,2}, Mingxing Wang^{1,2}  & Ji She^{1,2} 

Xenotropic and polytropic retrovirus receptor 1 (XPR1) functions as a phosphate exporter and is pivotal in maintaining human phosphate homeostasis. It has been identified as a causative gene for primary familial brain calcification. Here we present the cryogenic electron microscopy (cryo-EM) structure of human XPR1 (HsXPR1). HsXPR1 exhibits a dimeric structure in which only TM1 directly constitutes the dimer interface of the transmembrane domain. Each HsXPR1 subunit can be divided spatially into a core domain and a scaffold domain. The core domain of HsXPR1 forms a pore-like structure, along which two phosphate-binding sites enriched with positively charged residues are identified. Mutations of key residues at either site substantially diminish the transport activity of HsXPR1. Phosphate binding at the central site may trigger a conformational change at TM9, leading to the opening of the extracellular gate. In addition, our structural analysis reveals a new conformational state of HsXPR1 in which the cytoplasmic SPX domains form a V-shaped structure. Altogether, our results elucidate the overall architecture of HsXPR1 and shed light on XPR1-mediated phosphate export.

Inorganic phosphate (Pi) is vital to numerous physiological processes, including bone mineralization, signal transduction, and the synthesis of nucleic acids (DNA and RNA) as well as cell membranes (phospholipids)^{1,2}. Xenotropic and polytropic retrovirus receptor 1 (XPR1) was initially recognized as the receptor for xenotropic and polytropic murine leukemia viruses^{3–5}. Subsequently, it has been identified as a crucial transporter protein in maintaining phosphate homeostasis⁶. Unlike the sodium-dependent phosphate importers belonging to the SLC20 and SLC34 families⁷, XPR1 distinctively facilitates the efflux of phosphate⁶. XPR1 has been shown to have phosphate efflux activity across diverse species, including fruit fly, zebrafish, opossum, cat, and human⁶.

Given its phosphate transport activity, XPR1 is associated with various physiological processes and diseases. *Xpr1*-null mice exhibited embryonic lethality, and mice with conditional inactivation of *Xpr1* in renal tubules displayed generalized proximal tubular dysfunction and developed hypophosphatemic rickets⁸. Similar to phosphate

transporters from the SLC20 family, *Xpr1* is recognized as a causative gene for primary familial brain calcification (also known as idiopathic basal ganglia calcification or Fahr's disease)^{9–13}. This rare neurological disorder is characterized by calcium phosphate deposits in the basal ganglia and other brain regions. Furthermore, XPR1 plays a pivotal role in thrombosis, as evidenced by platelet-specific *XPR1*-deficient mice accumulating polyphosphate and exhibiting an increased risk of thrombosis¹⁴. A recent study revealed that inhibiting XPR1-dependent phosphate efflux leads to a toxic buildup of intracellular phosphate and growth inhibition in SLC34A2-high cancer cells, highlighting XPR1 as a promising therapeutic target for ovarian and uterine cancer¹⁵.

XPR1 comprises a transmembrane domain (TMD), an N-terminal cytoplasmic SPX (SYG1/PHO81/XPR1) domain, and a C-terminal loop. The SPX domain can bind inositol polyphosphate signaling molecules (InsPs) and is involved in the regulation of phosphate homeostasis^{16–21}. It's worth noting that XPR1 is the sole protein that contains an SPX domain in mammals, whereas multiple SPX domain-containing

¹MOE Key Laboratory for Cellular Dynamics, Hefei National Research Center for Interdisciplinary Sciences at the Microscale, Center for Advanced Interdisciplinary Science and Biomedicine of IHM, Division of Life Sciences and Medicine, University of Science and Technology of China, Hefei, China. ²Biomedical Sciences and Health Laboratory of Anhui Province, University of Science and Technology of China, Hefei, China. ✉ e-mail: wmx@ustc.edu.cn; jishe@ustc.edu.cn

proteins exist in yeast and plants^{18,22,23}. Despite its profound physiological significance, only the structure of the SPX domain of human XPR1 has been previously reported¹⁹. Many questions, such as the overall architecture of XPR1 and the mechanism underlying its phosphate transport, remain unanswered.

In this work, we perform structural and functional analyses of human XPR1 (HsXPR1), providing insights into its dimeric architecture and the mechanism of phosphate export.

Results

Overall structure of HsXPR1

Full-length HsXPR1 was recombinantly expressed in HEK293F cells, and its phosphate transport activity was evaluated using an *in vitro* phosphate assay, as detailed in the Methods section. Initially, we measured the Pi efflux from the untreated cells and observed only weak signals (Supplementary Fig. 1). Given that previous reports have indicated that Pi pre-treatment enhances the Pi efflux signal^{6,17}, we modified the phosphate transport assay by pretreating HEK293F cells with 10 mM Pi. Strikingly, the Pi export was observed to be several-fold higher than in cells without Pi pre-treatment (Fig. 1a, b and Supplementary Fig. 1). Since high extracellular phosphate levels are known to increase intracellular InsPs^{20,21}, the increased signal likely represents the Pi export by InsPs-activated HsXPR1. Importantly, cells over-expressing wild-type HsXPR1 exhibited significantly greater phosphate export compared to control cells (Fig. 1a, b), verifying the transport activity of recombinant HsXPR1.

The HsXPR1 structure was determined in the presence of phosphate at a resolution of 3.55 Å using single-particle cryogenic electron microscopy (cryo-EM) (Fig. 1c, Supplementary Fig. 2 and Supplementary Table S1). The cryo-EM map of HsXPR1 is of sufficient quality for the model building of the majority of the transmembrane domain (TMD), although the cytoplasmic domain remains unresolved (Fig. 1d, Supplementary Fig. 3). HsXPR1 forms a homodimer (Fig. 1c, d), and each subunit contains 10 transmembrane segments (TM1-TM10)

(Fig. 1e). Both the N- and C-termini of the TMD reside in the cytosol. The TMD can be separated into two distinct regions: a scaffold domain (TM1-TM4) and a core domain (TM5-TM10). The scaffold domain facilitates dimerization, while the core domain is responsible for ion conduction. The two domains are connected by the TM4-5 linker, a helix that runs nearly parallel to the cell membrane (Fig. 1e, f). Interestingly, a lipid molecule is lodged in a large cavity between the scaffold and core domains, surrounded by the TM4-5 linker and TM2-TM5 (Fig. 1f). This lipid seems to be essential for maintaining the structural integrity of XPR1, and it is tentatively designated as phosphatidylcholine, although its specific identity remains elusive. Additionally, several other lipid-shaped densities surround the transmembrane domain of HsXPR1 (Fig. 1c). Database searches with the TM-align server indicated that the region encompassing TM2 and TM5-10 of HsXPR1 resembles a microbial rhodopsin, NM-R3, with an RMSD of 4.1 Å over 208 residues^{24,25} (Supplementary Fig. 4). This finding aligns with previous research suggesting that XPR1 is an atypical G Protein-Coupled Receptor^{5,26}. However, a notable difference between HsXPR1 and rhodopsin is that TM2 and TM5-10 are split into two parts in sequence, likely indicating a different evolutionary origin.

Dimer interface of HsXPR1

The homodimerization of HsXPR1 in the current TMD structure is mediated by scaffold domains (Fig. 2a, b). The dimer interface is formed only by TM1, while TM2-TM4 provide critical support for stabilizing TM1. Specifically, the intracellular segment of TM1 contains several residues with small side chains, including Thr234, Gly238, Gly242, and Val246 (Fig. 2c). These residues engage in strong van der Waals interactions with residues from the adjacent subunit. In contrast, the extracellular portions of TM1 are distant from each other, and some lipid-like densities are discernible near the gap (Fig. 2a, b), further aiding in dimer formation. TM3 supports the dimer-forming TM1, primarily through hydrophobic interactions along the transmembrane helix (Supplementary Fig. 5). Moreover, a salt bridge exists between

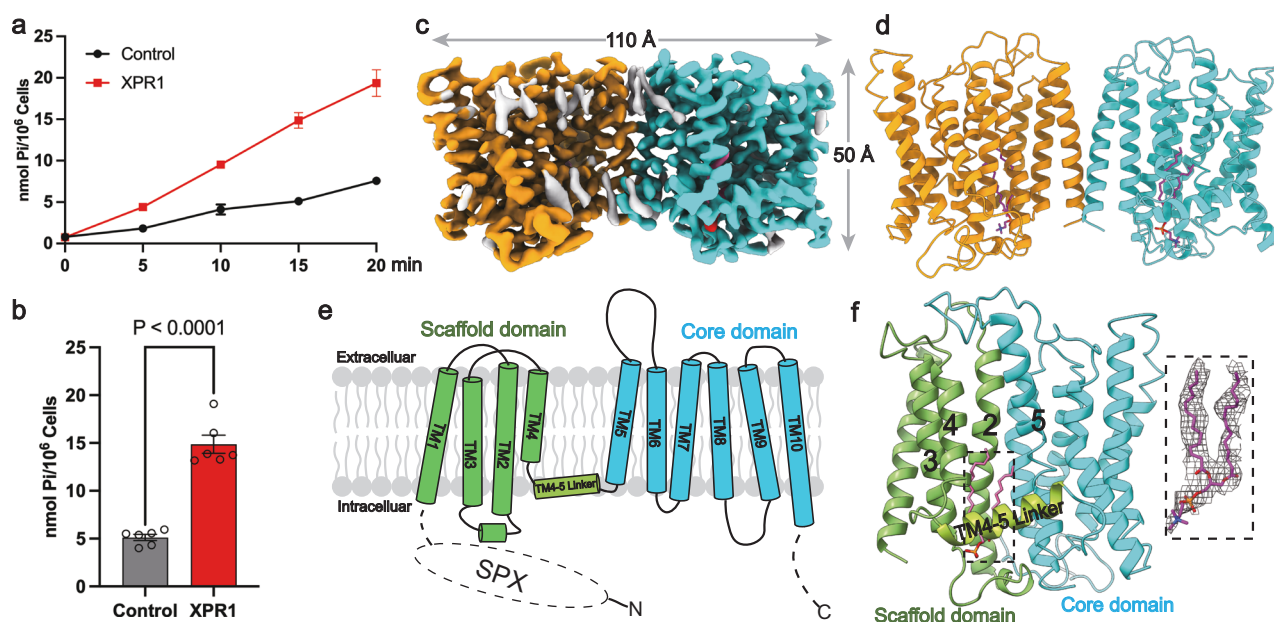


Fig. 1 | Functional and structural analysis of XPR1. **a** Time-dependent phosphate export activity of cells transfected with wild-type HsXPR1 (WT) or empty vector (control). The data points are the mean \pm s.e.m. ($n = 6$ independent experiments). **b** Phosphate export of HsXPR1 at 15 min from (a). P value from the two-tailed t -test is indicated on the bar chart. The data points are the mean \pm s.e.m. ($n = 6$ independent experiments). **c**, **d** Cryo-EM density map (c) and cartoon representation

(d) of XPR1 with each subunit depicted in an individual color. Lipid-like densities are colored gray. **e** The topology of XPR1. Dashed lines indicate the missing structural elements. **f** Structure of one XPR1 subunit. The scaffold domain (TM1-TM4) and core domain (TM5-TM10) are colored green and cyan, respectively. The potential phosphatidylcholine (purple) and its magnified EM density map (right panel) are shown.

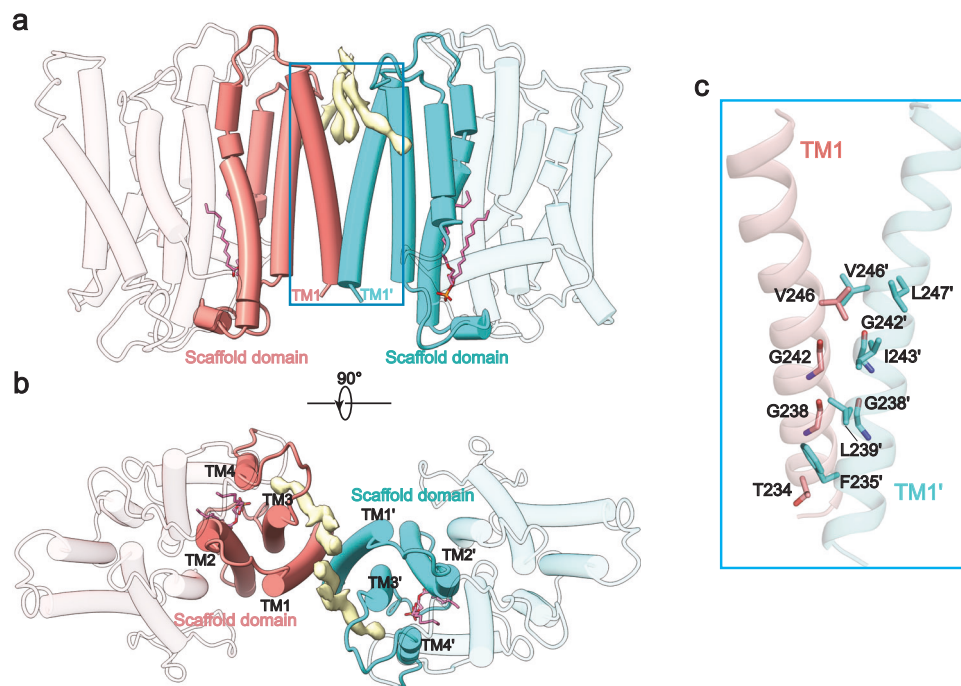


Fig. 2 | Scaffold domains mediate the dimerization of XPR1 subunits. a, b The dimer interface of the TMD is shown in the side (a) and top (b) views. The apostrophes denote the transmembrane helix from the neighboring subunit. Core

domains are shown as transparent. The lipid-like densities are colored yellow. **c** Detailed interactions at the dimer interface. Only half of the symmetric interactions are shown for clarity.

Arg236 from TM1 and Glu318 from TM3, and Glu318 is also hydrogen-bonded to Tyr367 from the loop between TM4 and the TM4-5 linker (Supplementary Fig. 5). On the other side, TM3 interacts with both TM2 and TM4, which bridge the scaffold and core domains (Fig. 2b). Homodimerization mediated by a single TM makes HsXPR1 a unique homodimeric structure.

Phosphate binding sites

To understand the ion recognition and transport mechanism of HsXPR1, we analysed its phosphate binding sites. The core domain of HsXPR1 (TM5-TM10) forms a pore-like structure within each TMD of the dimeric HsXPR1 (Fig. 3a), facilitating anion conduction. We employed AutoDock Vina to dock phosphate ions and identified the two most plausible binding sites, termed the external and central binding sites (Fig. 3a). The external phosphate site is situated on the extracellular side of the ion conduction pathway. Notably, a non-protein density peak is evident at this site in the EM map, exhibiting an intensity of -12σ (Supplementary Fig. 3). This site contains several positively charged residues, including Arg270 and Arg273 from TM2 and Arg448 from TM6 (Fig. 3b), which form a pocket with a positive surface electrostatic potential to accommodate the phosphate ion (Fig. 3c). Additionally, Thr580 from TM9 is close to the external phosphate (Fig. 3b). The positively charged residues within the binding site are stabilized by adjacent residues: Arg270 is sandwiched between Asp590 and Tyr412, while Arg273 forms a salt bridge with Asp409 (Fig. 3b). The residues at the external site are largely conserved from insects to mammals (Supplementary Fig. 6). We performed mutagenesis studies to evaluate the functional significance of residues around the external binding site. Alanine substitutions (R270A, D409A, Y412A, or R448A) profoundly reduced phosphate export (Fig. 3d), showing their functional significance.

The central binding site, located near the center of the pathway, comprises basic residues such as Lys482 from TM7, Arg570 from TM9, and Arg603 and Arg604 from TM10 (Fig. 3e, f). Although no phosphate density was observed in the current map, these residues form a positively charged site, which is ideal for binding negatively charged

phosphate. In the same layer, two residues partially neutralize and stabilize the binding site: Asp398 from TM5 forms a salt bridge with Arg604, and Tyr483 from TM7 interacts with Lys482. Below, Asp529, Asp566, and Trp607 further stabilize the cluster of arginines (Fig. 3f). Importantly, mutations at this site, including D398A, K482A, Y483A, R570A, R603A, and R604A, all led to a decrease in transport activity (Fig. 3g), indicating their critical roles in substrate recognition. The binding sites in HsXPR1 differ from that in SLC20A1. In the structure of bacterial SLC20A1²⁷, the absence of lysines or arginines, coupled with the presence of two negatively charged residues, necessitates sodium ions for phosphate recognition. In contrast, the predominantly positively charged binding sites in HsXPR1 suggest that it may directly bind phosphate.

Extracellular gate

The extracellular gate of HsXPR1 is primarily formed by interactions between TM9 and TM5-7 in the HsXPR1 structure (Fig. 4a). TM9 appears as a nearly straight helix that inserts into the cleft between TM8 and TM10. Its extracellular segment extensively interacts with TM5-TM7 (Fig. 4a, b), resulting in a closed extracellular gate. This closed extracellular gate can be delineated into three distinct layers (Fig. 4b). The first layer comprises Trp573 from TM9, which interacts with Asn401 from TM5, Thr486 from TM7, and Glu600 from TM10. The second layer primarily consists of Ile577 from TM9 interacting with Ser404 from TM5, Gln452 from TM6, and Met489 and Val490 from TM7. The third layer involves Thr582 and Thr583 from TM9, which form hydrogen bonds with Ser497 from TM7 and Tyr445 from TM6, respectively. Interestingly, the mutation in Trp573 of TM9 resulted in slightly greater export activity (Fig. 3d), which contradicts the results reported by others^{28,29}. To investigate this discrepancy, we conducted the Pi export assay without Pi pre-treatment for the Trp573Ala mutant. The results showed reduced export activity (Supplementary Fig. 7). This difference is thus attributed to the Pi treatment, although the mechanism remains to be further elucidated. Nonetheless, it is evident that the Trp573 residue plays an important role in the Pi transport of HsXPR1.

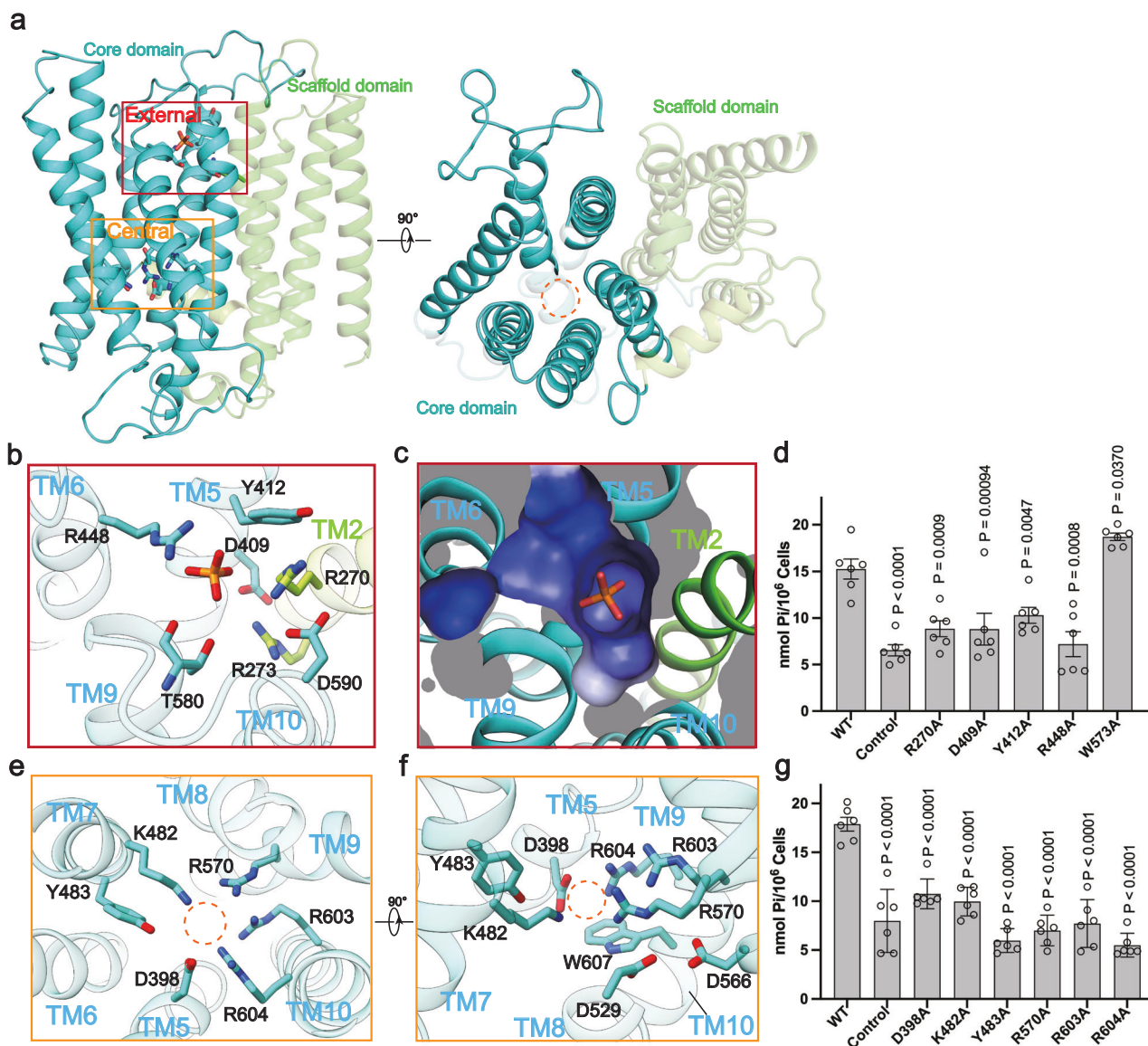


Fig. 3 | Phosphate binding by XPR1. **a** Two potential phosphate binding sites of XPR1 are marked by squares. The scaffold domain (TM1–TM4) and core domain (TM5–TM10) are colored in green and cyan, respectively. **b** A zoomed-in view of the external phosphate binding site. **c** Surface electrostatic potential of the external binding site. **d** Transport activity of XPR1 variants with point mutations at the

external site. *P* values from the two-tailed t-test are indicated on the bar chart.

e, f Zoomed-in views of the central phosphate binding site from the cytosol (**e**) and the side (**f**). **g** Transport activity of XPR1 variants with point mutations at the central site. The data points are the mean \pm s.e.m. ($n = 6$ independent experiments). *P* values from the two-tailed t-test are indicated on the bar chart.

Different from our structure of HsXPR1, the structure of XPR1^{open} (PDB: 8X5E)²⁸ clearly exhibited an open extracellular gate (Fig. 4c, d), with the extracellular segment of TM9 in XPR1^{open} swinging up by approximately 53 degrees (Fig. 4e, f). TM9 is thus a critical regulatory element for phosphate export. In our structure, Trp573 from TM9 forms the first layer of the extracellular gate, impeding phosphate export (Fig. 4b). However, in XPR1^{open}, it shifts by ~ 6 Å and forms a pi-pi stacking interaction with Tyr518 from TM8 (Fig. 4f), which contributes to stabilizing the open extracellular gate. The motion is hinged near Arg570 (Fig. 4f), a residue that makes up the central phosphate binding site (Fig. 3e, f), directly linking phosphate binding to the XPR1 gating. In line with the essential role of Arg570, the Arg570Cys mutation has been associated with primary familial brain calcification¹¹ (Supplementary Fig. 8).

Discussion

XPR1 is a phosphate exporter crucial for maintaining phosphate homeostasis in animals. In this study, we determined the structure of

human XPR1. HsXPR1 exhibits a dimeric structure in which only TM1 directly constitutes the dimer interface of the TMD. Two phosphate binding sites enriched with positively charged residues have been identified along the core domain of HsXPR1. The structural comparison reveals a major conformational change occurred at TM9, where the swing-up of TM9 opens the ion conduction pore. In this way, HsXPR1 may operate via a channel-like transport mechanism. During the manuscript review, several similar articles were published or released in bioRxiv^{28–32}. Overall, we share similar conclusions on the dimeric architecture, ion binding sites, and transport mechanism. However, our structural analysis reveals a HsXPR1 structure with a SPX dimer state, which will be discussed below.

Previous studies have highlighted the regulatory role of InsPs on XPR1 through binding to its SPX domain^{17,19}. During our data processing, we observed a cryo-EM map with enhanced densities of the SPX domain in the absence of exogenous InsPs, named HsXPR1^{SPX}, which can be reasonably fitted with the known structure of the SPX domain¹⁹ (Supplementary Figs. 9, 10). The SPX domains in HsXPR1^{SPX} form a

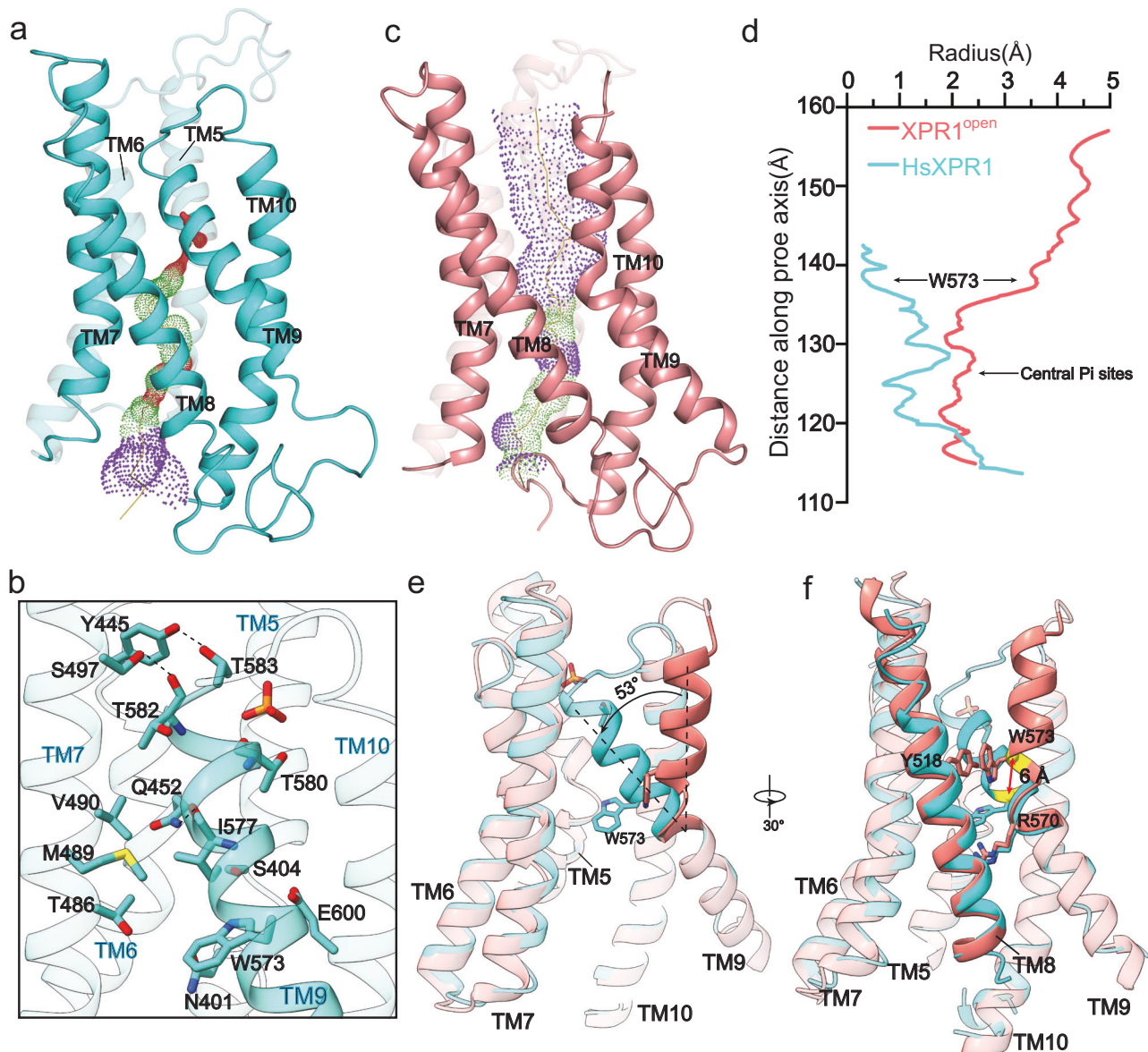


Fig. 4 | Extracellular gate of XPR1. a Ion conduction pathway of HsXPR1 calculated by the Hole program. **b** The interactions between TM9 and TM5-7. **c** Ion conduction pathway of XPR1^{open} (PDB: 8XSE) calculated by Hole program. **d** Pore radii of HsXPR1 and XPR1^{open}. W573 and the central Pi binding site are indicated by black arrows. The

pore radii of HsXPR1 and XPR1^{open} are shown in cyan and salmon, respectively. **e, f** Structural comparison between HsXPR1 and XPR1^{open} (PDB: 8XSE). Y518, R570, and W573 are shown in stick. For clarity, TM8s are not shown in (e).

V-shaped dimeric structure with a single contact site (Fig. 5a). This is different from the antiparallel or twisted dimer structure as reported in previous studies^{28,29} (Fig. 5b). The HsXPR1^{SPX} structure may represent one intermediate state of HsXPR1, in which the V-shaped SPX dimer can assist in stabilizing the HsXPR1 dimeric architecture and poises to allow the InsPs binding. When the cells detect a high concentration of phosphate and XPR1 is stimulated by InsPs, the SPX domains undergo a shift with respect to each other, and the N-terminal end of each SPX domain rotates approximately 35 degrees towards the transmembrane domain (Fig. 5b, c). This then relieves the pore blocking by the C-terminal loop as suggested previously by other groups^{28,30}. The phosphate gradient and membrane potential drive the phosphate efflux. The binding of intracellular phosphate to the central site triggers the movement of TM9, leading to the opening of the extracellular gate and the export of phosphate (Fig. 5c). Together, our studies offer valuable insights into the phosphate export mechanism of XPR1 and pave the way for future mechanistic studies.

Methods

Expression and purification of human XPR1

The DNA encoding human XPR1 (NCBI accession: NM_004736.4), including a C-terminal flag tag, was cloned into a pEZT-BM vector³³. The protein was expressed in HEK293F cells using the BacMam system (Thermo Fisher Scientific). Recombinant baculovirus was generated in Sf9 insect cells via the Bac-to-Bac system (Invitrogen), and P3 viruses were used for HEK293F cell transfection. HEK293F cells were cultured in SMM 293-TII medium (Sino Biological Inc.) at 37 °C and 5% CO₂. Sodium butyrate (at a final concentration of 10 mM) was added to boost protein expression. After 48–72 h, the cells were harvested by centrifugation at 3000 g for 15 min at 4 °C, resuspended in buffer A (20 mM Tris, pH 8.0, 150 mM NaCl), and homogenized by sonication on ice. A protease inhibitor cocktail (containing 2 µg/ml DNase I, 0.5 µg/ml pepstatin, 2 µg/ml leupeptin, 1 µg/ml aprotinin, and 0.1 mM PMSF) was added throughout the purification process. XPR1 was extracted with 1% (w/v) n-dodecyl-β-d-maltopyranoside (DDM,

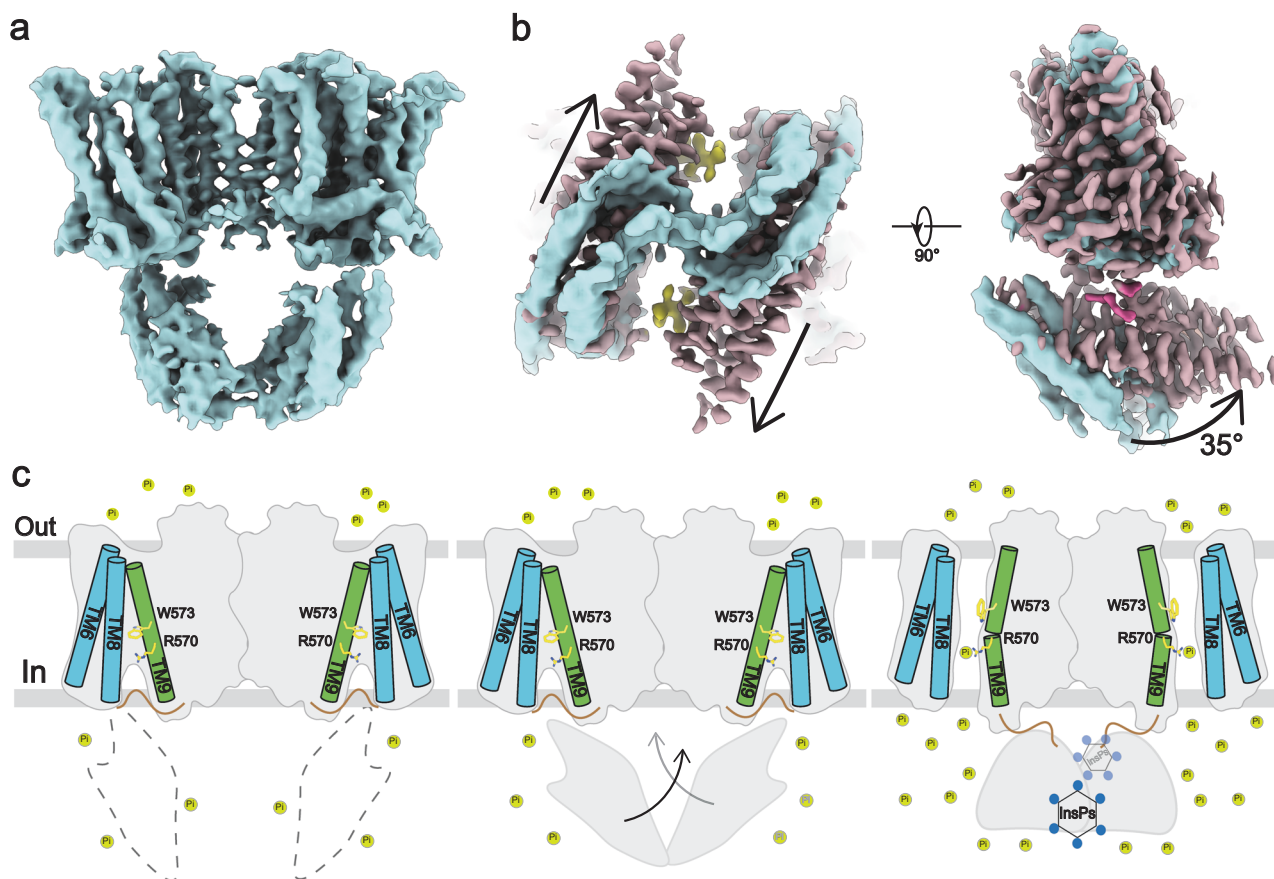


Fig. 5 | Transport mechanism of XPRI. **a** The electron microscopy density map of HsXPRI^{SPX}. **b** Comparison of HsXPRI^{SPX} (cyan) and XPRI^{InsP6} (salmon, EMD-38068) maps in different views. The InsP6 and C-terminal loop in the XPRI^{InsP6} map are shown in yellow and purple, respectively. **c** Working model for phosphate transport. When intracellular phosphate levels are low, HsXPRI can switch between

the flexible SPX state (left panel) and the V-shaped state (middle panel). When intracellular phosphate levels are high, InsPs binding leads to the rearrangement of the SPX domains and the activation of XPRI (right panel). Inorganic phosphate (Pi) is displayed as yellow spheres.

Anatrace) supplemented with 0.2% (w/v) cholesteryl hemisuccinate (Sigma Aldrich) by gentle agitation for 2 h. Following extraction, the supernatant was collected after 60 min of centrifugation at 30,000 g and purified using FLAG resin. During resin washing, the buffer was gradually changed to buffer B (20 mM Tris, pH 8.0, 150 mM NaCl, and 0.03% GDN). After elution with buffer B supplemented with 0.3 mg ml⁻¹ FLAG peptide, the protein was concentrated to a final volume of 500 µl and further purified by size exclusion chromatography on a Superose 6 10/300 GL column (GE Healthcare) equilibrated with buffer B.

Phosphate efflux assay

The phosphate concentration was determined by using the Malachite Green Phosphate Assay Kit (Sigma, MAK307). HEK293F cells were seeded at 1×10^6 cells per well in 2 ml of SMM 293-TII medium supplemented with 10% FBS in six-well plates. The cells were infected with 5% (v/v) P2 viruses expressing wild-type XPRI and its variants. After 12 h, sodium butyrate was added to boost protein expression, and the cells were incubated for an additional 12 h. For efflux measurements, unless otherwise indicated, Pi (NaH₂PO₄/Na₂HPO₄ mixture, pH 7.4, at 10 mM final concentration) was added to the culture and incubated for 30 min at 37 °C. Pi-incubated cells were gently washed three times with 1 ml of Krebs-HEPES buffer³⁴ (10 mM HEPES-NaOH, pH 7.4, 120 mM NaCl, 3 mM KCl, 2 mM CaCl₂, 2 mM MgCl₂, and 2 mM glucose, Pi-free), and then incubated in 1 ml of Krebs-HEPES buffer at 37 °C. Aliquots (8% v/v) of the supernatant were collected at 15 min or at other specified time points, and the Pi concentration was measured using the Malachite Green Phosphate Assay Kit. The P2 virus harboring the

empty vector was used as a negative control to calibrate the effect of the virus on the cells. Moreover, a series of Pi standards at 0, 1, 2.5, 5, 10, 20, 30, 40, and 50 µM were used to set up a standard curve. The absorbance at 620 nm was measured for each sample, and the amount of exported phosphate was determined from the standard curve. All the samples were run in 5 to 6 replicates.

Cryo-EM sample preparation and EM data acquisition

Cryo-EM grids were prepared by applying 3.5 µl of XPRI (at -8.0 mg/ml) with 1 mM Na₂HPO₄ in GDN buffer to glow-discharged holey carbon grids (Quantifoil Cu R2/1, 200 mesh). Grids were blotted for 3.0 s under 100% humidity at 4 °C before being plunged into liquid ethane using a Mark IV Vitrobot (Thermo Fisher Scientific). Micrographs were acquired on a Titan Krios microscope (Thermo Fisher Scientific) operated at 300 kV with a K3 Summit direct electron detector (Gatan). Images were recorded with EPU software (Thermo Fisher Scientific) in counting mode with a pixel size of 0.82 Å. The defocus range was set from -1.5 to -2.7 µm. Each micrograph was dose-fractionated into 30 frames at a dose rate of -18.7 e⁻/Å²/s, with a total exposure time of 3 s.

Image processing

Data processing was performed using the software package cryoSPARC³⁵. Micrographs were motion corrected with patch motion correction. The CTF parameters of the micrographs were estimated using patch CTF estimation. Two datasets were collected for the same sample. For dataset I, 1,356,043 particles were automatically picked and extracted from 2900 micrographs. After two rounds of 2D

classification, 316,973 particles were chosen for ab-initio reconstruction. 187,892 particles assigned to the good classes were selected for further refinement. For dataset II, 2,119,982 particles were picked from 5490 micrographs. After two rounds of 2D classification and one round of heterogeneous refinement, 1,241,608 particles from dataset II were chosen and merged with the 187,892 particles from dataset I. The combined dataset underwent four rounds of heterogeneous refinement. The good class was then selected for three parallel ab-initio reconstructions (initial resolution: 6 Å; maximum resolution: 4.5 Å). After removing duplicates, 424,758 particles were subjected to a final round of non-uniform refinement with C2 symmetry imposed, yielding a map at a resolution of 3.55 Å.

Dataset II was further processed by using Relion⁴³⁶. Motion correction was performed using the MotionCorr2 program³⁷, and the contrast transfer function parameters of the micrographs were estimated using the Gctf program³⁸. A total of 4201 micrographs were kept for further data processing. 2,369,078 particles were automatically picked and extracted with a binning factor of 3 for 2D classification. A total of 1,618,520 particles were selected for two successive rounds of 3D classifications. 345,317 particles exhibiting strong SPX domain density were selected and re-extracted. After 3D refinement with C2 symmetry and particle polishing, the final map of HsXPR1^{SPX} was reconstructed to a resolution of 4.3 Å.

Model building, refinement, and validation

Model building was conducted in Coot³⁹ and the XPR1 model predicted by AlphaFold2⁴⁰ was used as an initial reference. Real-space model refinement⁴¹ and validation⁴² were performed in Phenix. The final structural model contains residues 230–618. The pore radius was calculated using the HOLE⁴³ program. Figures were prepared using PyMol⁴⁴ and ChimeraX⁴⁵ software.

Statistical analysis

Statistical analysis was performed using GraphPad Prism 8.0. Data from the XPR1 transport assay are presented as the mean ± s.e.m., and statistical significance was determined using the two-tailed t-test.

Molecular docking

AutoDock Vina⁴⁶ was used for molecular docking analysis of the HsXPR1 structure with PO₄³⁻. Ligand and receptor files were prepared using AutodockTools⁴⁷. Docking was performed using a cubic box encompassing the binding pocket. The models with the high binding affinity were further analysed.

Reporting summary

Further information on research design is available in the Nature Portfolio Reporting Summary linked to this article.

Data availability

The data that support this study are available from the corresponding authors upon request. Cryo-EM maps have been deposited in the Electron Microscopy Data Bank (EMDB) under accession codes EMD-60469 (HsXPR1) [<https://www.ebi.ac.uk/pdbe/entry/emdb/EMD-60469>] and EMD-62621 (HsXPR1^{SPX}) [<https://www.ebi.ac.uk/pdbe/entry/emdb/EMD-62621>]. The atomic coordinates have been deposited in the Protein Data Bank (PDB) under accession codes 8ZTO (HsXPR1) [<https://doi.org/10.2210/pdb8ZTO/pdb>]. The source data underlying Figs. 1a, 1b, 3d, 3g, and Supplementary Figs. 1 and 8 are provided as a Source Data file. The sequence of human XPR1 is available through NCBI accession NM_004736.4. Source data are provided with this paper.

References

- Hernando, N., Gagnon, K. & Lederer, E. Phosphate transport in epithelial and nonepithelial tissue. *Physiol. Rev.* **101**, 1–35 (2021).
- Michigami, T., Kawai, M., Yamazaki, M. & Ozono, K. Phosphate as a signaling molecule and its sensing mechanism. *Physiol. Rev.* **98**, 2317–2348 (2018).
- Yang, Y. L. et al. Receptors for polytropic and xenotropic mouse leukaemia viruses encoded by a single gene at. *Nat. Genet.* **21**, 216–219 (1999).
- Taylor, C. S., Nouri, A., Lee, C. G., Kozak, C. & Kabat, D. Cloning and characterization of a cell surface receptor for xenotropic and polytropic murine leukemia viruses. *Proc. Natl. Acad. Sci. USA* **96**, 927–932 (1999).
- Battini, J. L., Rasko, J. E. J. & Miller, A. D. A human cell-surface receptor for xenotropic and polytropic murine leukemia viruses: possible role in G protein-coupled signal transduction. *Proc. Natl. Acad. Sci. USA* **96**, 1385–1390 (1999).
- Giovannini, D., Touhami, J., Charnet, P., Sitbon, M. & Battini, J. L. Inorganic phosphate export by the retrovirus receptor XPR1 in metazoans. *Cell Rep.* **3**, 1866–1873 (2013).
- Biber, J., Hernando, N. & Forster, I. Phosphate transporters and their function. *Annu. Rev. Physiol.* **75**, 535–550 (2013).
- Ansermet, C. et al. Renal fanconi syndrome and hypophosphatemic rickets in the absence of xenotropic and polytropic retroviral receptor in the nephron. *J. Am. Soc. Nephrol.* **28**, 1073–1078 (2017).
- Legati, A. et al. Mutations in XPR1 cause primary familial brain calcification associated with altered phosphate export. *Nat. Genet.* **47**, 579–581 (2015).
- Lopez-Sanchez, U. et al. Characterization of XPR1/SLC53A1 variants located outside of the SPX domain in patients with primary familial brain calcification. *Sci. Rep.* **9**, 6776 (2019).
- Guo, X. X. et al. Spectrum of SLC20A2, PDGFRB, PDGFB and XPR1 mutations in a large cohort of patients with primary familial brain calcification. *Hum. Mutat.* **40**, 392–403 (2019).
- Ramos, E. M. et al. Primary brain calcification: an international study reporting novel variants and associated phenotypes. *Eur. J. Hum. Genet.* **26**, 1462–1477 (2018).
- Anheim, M. et al. XPR1 mutations are a rare cause of primary familial brain calcification. *J. Neurol.* **263**, 1559–1564 (2016).
- Mailer, R. K. et al. Xenotropic and polytropic retrovirus receptor 1 regulates procoagulant platelet polyphosphate. *Blood* **137**, 1392–1405 (2021).
- Bondeson, D. P. et al. Phosphate dysregulation via the XPR1-KIDINS220 protein complex is a therapeutic vulnerability in ovarian cancer. *Nat. Cancer* **3**, 681–695 (2022).
- Azevedo, C. & Saiardi, A. Eukaryotic phosphate homeostasis: the inositol pyrophosphate perspective. *Trends Biochem. Sci.* **42**, 219–231 (2017).
- Li, X. Y. et al. Control of XPR1-dependent cellular phosphate efflux by InsP is an exemplar for functionally-exclusive inositol pyrophosphate signaling. *Proc. Natl. Acad. Sci. USA* **117**, 3568–3574 (2020).
- Wilson, M. S., Jessen, H. J. & Saiardi, A. The inositol hexakisphosphate kinases IP6K1 and-2 regulate human cellular phosphate homeostasis, including XPR1-mediated phosphate export. *J. Biol. Chem.* **294**, 11597–11608 (2019).
- Wild, R. et al. Control of eukaryotic phosphate homeostasis by inositol polyphosphate sensor domains. *Science* **352**, 986–990 (2016).
- López-Sánchez, U. et al. Interplay between primary familial brain calcification-associated SLC20A2 and XPR1 phosphate transporters requires inositol polyphosphates for control of cellular phosphate homeostasis. *J. Biol. Chem.* **295**, 9366–9378 (2020).
- Gu, C. et al. The Significance of the Bifunctional Kinase/Phosphatase Activities of Diphosphoinositol Pentakisphosphate Kinases (PPIP5Ks) for coupling inositol pyrophosphate cell signaling to cellular phosphate homeostasis. *J. Biol. Chem.* **292**, 4544–4555 (2017).
- Jung, J. Y., Ried, M. K., Hothorn, M. & Poirier, Y. Control of plant phosphate homeostasis by inositol pyrophosphates and the SPX domain. *Curr. Opin. Biotechnol.* **49**, 156–162 (2018).

23. Secco, D., Wang, C., Shou, H. & Whelan, J. Phosphate homeostasis in the yeast *Saccharomyces cerevisiae*, the key role of the SPX domain-containing proteins. *FEBS Lett.* **586**, 289–295 (2012).
24. Yun, J. H. et al. Pumping mechanism of NM-R3, a light-driven bacterial chloride importer in the rhodopsin family. *Sci. Adv.* **6**, eay2042 (2020).
25. Zhang, Y. & Skolnick, J. TM-align: a protein structure alignment algorithm based on the TM-score. *Nucleic Acids Res.* **33**, 2302–2309 (2005).
26. Vaughan, A. E., Mendoza, R., Aranda, R., Battini, J. L. & Miller, A. D. Xpr1 is an atypical G-Protein-coupled receptor that mediates xenotropic and polytropic murine retrovirus neurotoxicity. *J. Virol.* **86**, 1661–1669 (2012).
27. Tsai, J. Y. et al. Structure of the sodium-dependent phosphate transporter reveals insights into human solute carrier SLC20. *Sci. Adv.* **6**, eabb4024 (2020).
28. Yan, R. et al. Human XPR1 structures reveal phosphate export mechanism. *Nature* **633**, 960–967 (2024).
29. Lu, Y. et al. Structural basis for inositol pyrophosphate gating of the phosphate channel XPR1. *Science* **386**, eadp3252 (2024).
30. He, Q. et al. Structural basis of phosphate export by human XPR1. *Nat. Commun.* **16**, 683 (2025).
31. Zhang, W. et al. Structural insights into the mechanism of phosphate recognition and transport by XPR1. *Nat. Commun.* **16**, 18 (2025).
32. Zhu, Q., Yaggi, M. F., Jork, N., Jessen, H. J. & Diver, M. M. Transport and InsP8 activation mechanisms of the human inorganic phosphate exporter XPR1. *bioRxiv*, 2024.10.04.616715 (2024).
33. Morales-Perez, C. L., Noviello, C. M. & Hibbs, R. E. Manipulation of subunit stoichiometry in heteromeric membrane proteins. *Structure* **24**, 797–805 (2016).
34. Bhat, S. et al. A mechanism of uncompetitive inhibition of the serotonin transporter. *Elife* **12**, e82641 (2023).
35. Punjani, A., Rubinstein, J. L., Fleet, D. J. & Brubaker, M. A. cryoSPARC: algorithms for rapid unsupervised cryo-EM structure determination. *Nat. Methods* **14**, 290–296 (2017).
36. Kimanius, D., Dong, L., Sharov, G., Nakane, T. & Scheres, S. H. W. New tools for automated cryo-EM single-particle analysis in RELION-4.0. *Biochem J.* **478**, 4169–4185 (2021).
37. Zheng, S. Q. et al. MotionCor2: anisotropic correction of beam-induced motion for improved cryo-electron microscopy. *Nat. Methods* **14**, 331–332 (2017).
38. Zhang, K. Gctf: real-time CTF determination and correction. *J. Struct. Biol.* **193**, 1–12 (2016).
39. Emsley, P., Lohkamp, B., Scott, W. G. & Cowtan, K. Features and development of coot. *Acta Crystallogr.* **66**, 486–501 (2010).
40. Varadi, M. et al. AlphaFold protein structure database in 2024: providing structure coverage for over 214 million protein sequences. *Nucleic Acids Res.* **52**, D368–D375 (2024).
41. Afonine, P. V. et al. Real-space refinement in for cryo-EM and crystallography. *Acta Crystallogr.* **74**, 531–544 (2018).
42. Afonine, P. V. et al. New tools for the analysis and validation of cryo-EM maps and atomic models. *Acta Crystallogr.* **74**, 814–840 (2018).
43. Smart, O. S., Neduvilil, J. G., Wang, X., Wallace, B. A. & Sansom, M. S. P. HOLE: a program for the analysis of the pore dimensions of ion channel structural models. *J. Mol. Graph. Model.* **14**, 354 (1996).
44. Schrodinger, L. L. C. The PyMOL Molecular Graphics System, Version 1.8. (2015).
45. Goddard, T. D. et al. UCSF ChimeraX: meeting modern challenges in visualization and analysis. *Protein Sci.* **27**, 14–25 (2018).
46. Trott, O. & Olson, A. J. Software news and update autodock vina: improving the speed and accuracy of docking with a new scoring function, efficient optimization, and multithreading. *J. Comput. Chem.* **31**, 455–461 (2010).
47. Morris, G. M. et al. AutoDock4 and AutoDockTools4: automated docking with selective receptor flexibility. *J. Comput. Chem.* **30**, 2785–2791 (2009).

Acknowledgements

We thank the Cryo-EM Center at University of Science and Technology of China for the support of cryo-EM data collection. We thank Dr. Yongxiang Gao for assistance with cryo-EM data screening and collection. We thank Dr. Chunlei Cang and Dongyu Xu for their help and suggestions. This work was supported by the Ministry of Science and Technology of China (2021YFF0600801 to J.S.), the National Natural Science Foundation of China (GG2070000569 to J.S. and 32100967 to M.W.), and the Center for Advanced Interdisciplinary Science and Biomedicine of IHM (QYPY20220009 to J.S.).

Author contributions

J.S., M.W., and L.C. conceived the project; L.C. prepared the samples; L.C. and M.W. performed the data acquisition; L.C., M.W., J.H., and J.S. carried out the image processing and structure determination; L.C. conducted the functional studies; M.W. and J.S. supervised the project and revised the manuscript; and all the authors participated in the research design, data analysis, and manuscript preparation.

Competing interests

The authors declare no competing interests.

Additional information

Supplementary information The online version contains supplementary material available at <https://doi.org/10.1038/s41467-025-58195-6>.

Correspondence and requests for materials should be addressed to Mingxing Wang or Ji She.

Peer review information *Nature Communications* thanks Daohua Jiang and the other, anonymous, reviewer(s) for their contribution to the peer review of this work. A peer review file is available.

Reprints and permissions information is available at <http://www.nature.com/reprints>

Publisher's note Springer Nature remains neutral with regard to jurisdictional claims in published maps and institutional affiliations.

Open Access This article is licensed under a Creative Commons Attribution-NonCommercial-NoDerivatives 4.0 International License, which permits any non-commercial use, sharing, distribution and reproduction in any medium or format, as long as you give appropriate credit to the original author(s) and the source, provide a link to the Creative Commons licence, and indicate if you modified the licensed material. You do not have permission under this licence to share adapted material derived from this article or parts of it. The images or other third party material in this article are included in the article's Creative Commons licence, unless indicated otherwise in a credit line to the material. If material is not included in the article's Creative Commons licence and your intended use is not permitted by statutory regulation or exceeds the permitted use, you will need to obtain permission directly from the copyright holder. To view a copy of this licence, visit <http://creativecommons.org/licenses/by-nc-nd/4.0/>.

© The Author(s) 2025